22

Relativistic Nonlinear Thomson Scattering: Toward Intense Attosecond Pulse

Kitae Lee[1], Sang-Young Chung[2], and Dong-Eon Kim[3]
[1]*Korea Atomic Energy Research Institute,*
[2]*Pusan national University,*
[3]*Pohang University of Science and Technology*
Republic of Korea

1. Introduction

Over many millennia of human history, mankind has been interested in how events change in time, namely their dynamics. However, the time resolution of recording individual steps has been limited to direct sensory perception such as the eye's ability (0.1 sec. or so) to recognize the motion, until 1800 AD when the technical revolution occurred following the industrial revolution. A famous motion picture of a galloping horse by E. Muybridge in 1878 is a good example of the technological development in time-resolved measurement. By this time, the nanosecond time resolution has been achieved; however, it took another century to break the nanosecond barrier as shown in Fig.1. The Advent of a laser has paved ways to ever shorter time resolution: in the 1980's, the picosecond barrier was broken and the femtosecond science and technology has rapidly progressed in the 1990's; at the turn of the 21st century, the femtosecond barrier has been broken (Hantschel et al., 2001), opening up the era of attosecond science and technology. The current shortest duration of a pulse achieved is 80 attoseconds around 100 eV of photon energy (Goulielmakis et al., 2008).

Femtosecond science and technology have allowed us to explore various ultrafast phenomena in physical (Siders et al., 1999), chemical (Zewail, 2000) and biological (Vos et al., 1999) systems. A great number of ultrafast atomic motions in biology, chemistry, and physics have been investigated with optical probes. In physics, the nature of atomic re-arrangements during phase transitions and the relation between amorphous, liquid and crystalline states has been interest (Afonso et al., 1996; Huang et al., 1998). Along with much interest in spintronics during the last decade, efforts have been made to understand spin dynamics in various pure and complex magnetic systems. In chemistry, the real time observation of atomic motions in chemical reactions has been long thought for. Femtosecond optical and IR technology has served this purpose in excellent ways. Femtosecond pulses have pumped molecules to create wavepackets. The observation of the motion of the wavepackets using femtosecond pulse probe or other methods has provided rich information on chemical reactions (Zewail, 2000). The various chemical bonds such as covalent, ionic, dative, metallic, hydrogen and van der Waals bonds have been studied in the varying complexity of molecular systems from diatomics to proteins and DNA. All of

Source: Advances in Solid-State Lasers: Development and Applications, Book edited by: Mikhail Grishin,
ISBN 978-953-7619-80-0, pp. 630, February 2010, INTECH, Croatia, downloaded from SCIYO.COM

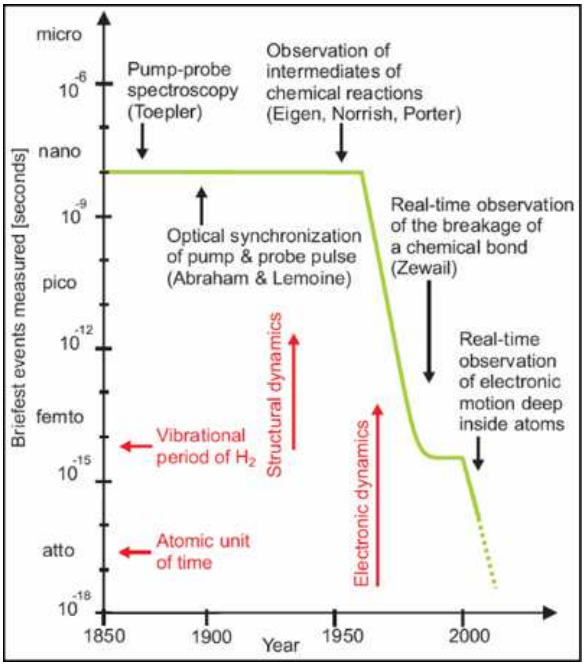

Fig. 1. Evolution of techniques for real-time observation of microscopic processes (Krausz et al., 2009).

these successful applications of femtosecond optical technology to follow reaction dynamics in chemistry have led to the award of Nobel prize to Prof. Zewail in 1999 who has initiated femtochemistry in the 1990's. There are also many fundamental biological processes taking place in femtosecond time scale. Good examples are photo-induced isomerizations (Gai et al., 1998) and ligand dissociations (Perutz et al., 1998). Femtosecond optical pulses have been used for the investigation of these processes.

During the last several years, isolated attosecond pulses have been successfully exploited to control the localization of electron under chemical reaction (Kling et al., 2006), observe inner shell transitions in atoms (Drescher et al., 2002), and electron tunneling across Coulomb barrier (Uiberacker et al., 2007), electron transport in condensed matter (Cavalieri et al., 2007).

The demand on and the emphasis to the understanding of the ultrafast phenomena and the control of them is ever increasing. The Department of Energy of the United States of America asked the Basic Energy Science Advisory Committee (BESAC) to identify grand challenges in science to be pursued in the 21st century. The BESAC has identified 5 grand challenges in their report, the summary of which has been published in the July issue of Physics Today in 2008 (Fleming & Ratner, 2008). The first of the grand challenges is to control material properties at the level of electronic motion. The report recommended the development of attosecond and femtosecond metrology to measure and control electron dynamics.

Optical or ultraviolet light allows one to probe the dynamical changes of excited electronic states in a sample. This is the core of interest in many research topics such as electron-hole dynamics in solids, or excitation transfer in photosynthesis, bond breaking in chemical

reactions. However, no or partial information on structure can be obtained if the process under investigation involves the structural changes.

X-ray imaging or diffraction has the potential to provide a global picture of structural changes in the fields of atomic and molecular physics, plasma physics, material science, chemistry and life science (Bloembergen, 1999; http://tesla.desy.de/new_pages /TDR_CD/PartV/fel.html). Since x-ray photons are scattered from all the electrons in a sample, the intensity of diffraction is directly related to the electronic density. Since the structural changes occur in the time scale of 100 fs or so, following the charge re-arrangement, the electronic density measured in this time scale closely reflects the atomic structure. On the other hand, attosecond x-ray pulse will enable us to follow even faster motions of electrons in intra-atomic or intra-molecular processes, which has not been achieved yet because of the lack of such sources.

Femtosecond time-resolved x-ray diffraction experiments have been used to study structural processes such as the observation of atomic structure and dynamics [18], the investigation of ultrafast phase transition in solid (Gaffney & Chapman, 2008) and time-resolved biomolecular imaging (Sokolowski-Tinten et al., 2003). These results are very impressive and of landmark: however, there are still many phenomena yet to be explored and a variety of attosecond and femtosecond X-ray sources yet to be further developed. They comprise a great challenge to the scientific community.

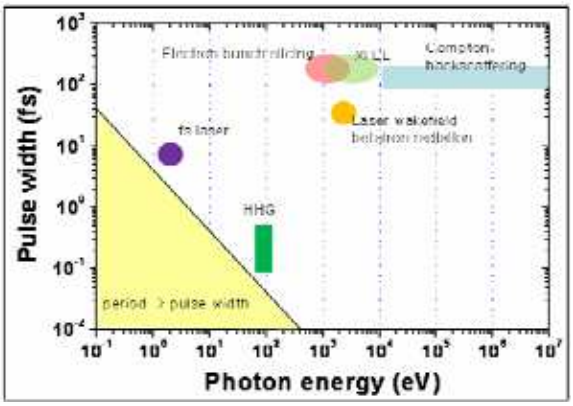

Fig. 2. Currently-available ultrafast light sources are plotted in terms of photon energy and pulse duration.

Figure 2 shows ultrafast sources available currently or in the immediate future. It is conspicuous that there is no source available in keV or higher energies faster than 10 fs. In fact, for wider exploration and manipulation of electron dynamics in a vast spectrum of natural phenomena, attosecond or a few fs keV pulses are demanded.

Several schemes have been proposed and/or demonstrated to generate an ultrashort keV x-ray pulse: the relativistic Doppler shift of a backscattered laser pulse by a relativistic electron beam (Sprangle et al., 1992; Hartemann, 1998; Esarey et al., 1993a; Chung et al., 2009), the harmonic frequency upshift of a laser pulse by relativistic nonlinear motion of electrons (Vachaspati, 1962; Brown & Kibble, 1964; Esarey et al,, 1992; Chen et al., 1998, 2000; Ueshima et al, 1999; Kaplan & Shkolnikov, 2002; Banerjee et al., 2002; Lee et al., 2003a, 2003b, 2005, 2008; Phuoc et al., 2003; Kim et al., 2009), high order harmonic generation in the interaction

of intense laser pulse with solids (Linde et al., 1995, 1996, 1999; Norreys et al., 1996; Lichters et al., 1996; Tarasevitch et al., 2000) and x-ray laser using inner shell atomic transitions (Kim et al., 1999, 2001).

Ultrafast high-intensity X-rays can be generated from the interaction of high intensity femtosecond laser via Compton backscattering (Hartemann et al., 2005), relativistic nonlinear Thomson scattering (Ueshima et al., 1999; Kaplan & Shkolnikov 2002; Banerjee et al., 2002) and laser-produced betatron radiation (Phuoc et al., 2007). In synchrotron facilities, electron bunch slicing method has been adopted for experiments (Schoenlein, 2000; Beaud et al., 2007). Moreover, X-ray free electron lasers (Normile, 2006) were proposed and have been under construction. The pulse duration of these radiation sources are in the order of a few tens to hundred fs. There are growing demands for new shorter pulses than 10 fs.

The generation of intense attosecond or femtosecond keV lights via Thomson scattering (Lee et al., 2008; Kim et al., 2009) is attractive, because the radiation is intense and quasi-monochromatic. This radiation may be also utilized in medical (Girolami et al., 1996) and nuclear physics (Weller & Ahmed, 2003) area of science and technology.

When a low-intensity laser pulse is irradiated on an electron, the electron undergoes a harmonic oscillatory motion and generates a dipole radiation with the same frequency as the incident laser pulse, which is called Thomson scattering. As the laser intensity increases, the oscillatory motion of the electron becomes relativistically nonlinear, which leads to the generation of harmonic radiations. This is referred to as **relativistic nonlinear Thomson scattered (RNTS) radiation**. The RNTS radiation has been investigated in analytical ways (Esarey et al., 1993a; Chung et al., 2009; Vachaspati, 1962; Brown et al., 1964; Esarey & Sprangle, 1992; Chen et al., 1998; Ueshima et al., 1999; Chen et al., 2000; Kaplan & Shkolnikov, 2002; Banerjee et al., 2002). Recently, such a prediction has been experimentally verified by observing the angular patterns of the harmonics for a relatively low laser intensity of 4.4×10^{18} W/cm^2 (Lee et al., 2003a, 2003b). Esarey *et al.* (Esarey et al., 1993a) has investigated the plasma effect on RNTS and presented a set of the parameters for generating a 9.4-ps x-ray pulse with a high peak flux of 6.5×10^{21} photons/s at 310 eV photon energy using a laser intensity of 10^{20} W/cm^2. Ueshima *et al.* (Ueshima et al., 1999) has suggested several methods to enhance the radiation power, using particle-incell simulations for even a higher intensity. Kaplan and Shkolnikov *et al.* (Kaplan & Shkolnikov, 2002) proposed a scheme for the generation of zeptosecond (10^{-21} sec) radiation using two counter-propagating circularly polarized lasers, named as lasertron.

Recently, indebted to the development of the intense laser pulse, experiments on RNTS radiation have been carried out by irradiating a laser pulse of 10^{18}–10^{20} W/cm^2 on gas jet targets (Kien et al., 1999; Paul et al., 2001; Hertz et al., 2001). A numerical study in the case of single electron has been attempted to characterize the RNTS radiation (Kawano et al., 1998) and a subsequent study has shown that it has a potential to generate a few attosecond x-ray pulse (Harris & Sokolov, 1998). Even a scheme for the generation of a zeptosecond x-ray pulse using two counter propagating circularly polarized laser pulses has been proposed (Kaplan & Shkolnikov, 1996).

In this chapter, we concern RNTS in terms of the generation of ultrafast X-ray pulses. The topics such as fundamental characteristics of RNTS radiations, coherent RNTS radiations, effects of the high-order fields (HOFs) under a tight-focusing condition, and generation of an intense attosecond x-ray pulse will be discussed in the following sections.

2. Fundamental characteristics of RNTS radiations

In this section, the dynamics of an electron under an ultra-intense laser pulse and some fundamental characteristics of the RNTS radiations will be discussed (Lee et al., 2003a, 2003b).

2.1 Electron dynamics under a laser pulse

The dynamics of an electron irradiated by a laser field is obtained from the relativistic Lorentz force equation:

$$\frac{d}{dt}\left(\gamma\vec{\beta}\right) = -\frac{e}{m_e c}\left(\vec{E}_L + \vec{\beta}\times\vec{B}_L\right), \tag{1}$$

The symbols used are: electron charge (e), electron mass (m_e), speed of light (c), electric field ($\vec{E}_L$), magnetic field ($\vec{B}_L$), velocity of the electron divided by the speed of light ($\vec{\beta}$), and relativistic gamma factor ($\gamma = 1/\sqrt{1-\beta^2}$). It is more convenient to express the laser fields with the normalized vector potential, $\vec{a} = e\vec{E}_L / m_e\omega_L c$, where ω_L is the angular frequency of the laser pulse. It can be expressed with the laser intensity I_L in W/cm² and the laser wavelength λ_L in micrometer as below:

$$a = 8.5\times10^{-10}\lambda_L\sqrt{I_L}\ . \tag{2}$$

Eq. (1) can be analytically solved under a planewave approximation and a slowly-varying envelope approximation, which lead to the following solution (Esarey et al., 1993a):

$$\gamma\vec{\beta} = \gamma_o\vec{\beta}_o + \vec{a} + \frac{a^2 + 2\gamma_o\vec{a}\cdot\vec{\beta}_o}{2q_o}\hat{z}\ , \tag{3}$$

$$\gamma = \frac{\left|\vec{a} + \gamma_o\vec{\beta}_{o\perp}\right|^2 + 1 + q_o^2}{2q_o}\ , \tag{4}$$

where $q_o = \gamma_o\left(1-\beta_{oz}\right)$ and the subscript $\perp$ denotes the direction perpendicular to the direction of laser propagation (+z). The subscript, 'o' denotes initial values. When the laser

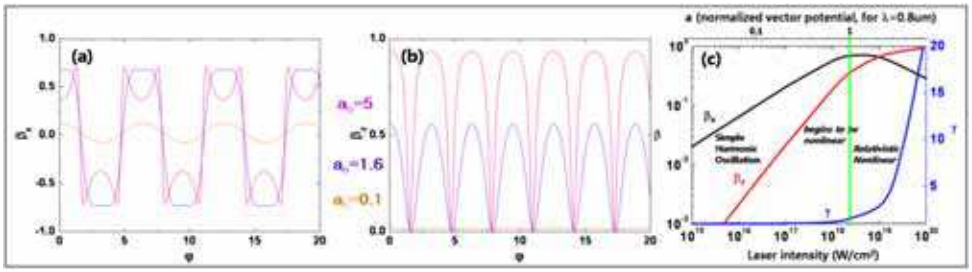

Fig. 3. Dynamics of an electron under a laser pulse: Evolution of (a) transverse and (b) longitudinal velocities, and (c) peak values on laser intensities. The initial velocity was set to zero for this calculation. Different colors correspond to different a_o's in (a) and (b).

intensity is low or $|a| << 1$, the electron conducts a simple harmonic oscillation but as the intensity becomes relativistic or $|a| \geq 1$, the electron motion becomes relativistically nonlinear. Figure 3 (a) and (b) show how the electron's oscillation becomes nonlinear due to relativistic motion as the laser intensity exceeds the relativistic intensity. One can also see that the drift velocity along the +z direction gets larger than the transverse velocity as $|a| \geq 1$ [Fig. 3 (c)].

2.2 Harmonic spectrum by a relativistic nonlinear oscillation

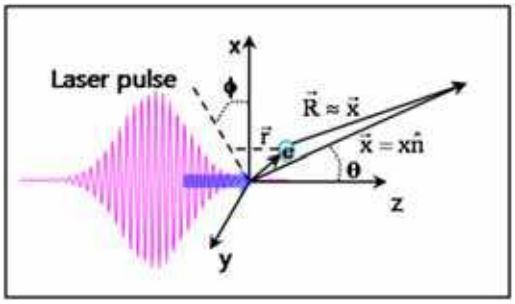

Fig. 4. Schematic diagram for the analysis of the RNTS radiations

Once the dynamics of an electron is obtained, the angular radiation power far away from the electron toward the direction, $\hat{n}$ [Fig. 4] can be obtained through the Lienard-Wiechert potential (Jackson, 1975)

$$\frac{dP(t)}{d\Omega} = \left|\vec{A}(t)\right|^2 \tag{5}$$

$$\vec{A}(t) = \sqrt{\frac{e^2}{4\pi c}}\left[\frac{\hat{n}\times\left\{\left(\hat{n}-\vec{\beta}\right)\times\dot{\vec{\beta}}\right\}}{\left(1-\hat{n}\cdot\vec{\beta}\right)^3}\right]_{t'} \tag{6}$$

where t′ is the retarded time and is related to t by

$$t = t' + \frac{x - \hat{n}\cdot\vec{r}(t')}{c}. \tag{7}$$

Then the angular spectrum is obtained by

$$\frac{d^2I}{d\omega d\Omega} = 2\left|\vec{A}(\omega)\right|^2, \tag{8}$$

where $\vec{A}(\omega)$ is the Fourier transform of $\vec{A}(t)$. These formulae together with Eq. (1) are used to evaluate the scattered radiations. Under a planewave approximation, the RNTS spectrum can be analytically obtained (Esarey et al., 1993a). Instead of reviewing the analytical process, important characteristics will be discussed along with results obtained in numerical simulations.

Figure 5 shows how the spectrum is changed, as the laser intensity gets relativistic. The spectra were obtained by irradiating a linearly-polarized laser pulse on a counter-propagating relativistic electron with energy of 10 MeV, which is sometimes called as nonlinear Compton backscattering. One can see that higher order harmonics are generated as the laser intensity increase. It is also interesting that the spacing between harmonic lines gets narrower, which is caused by Doppler effect (See below). The cut-off harmonic number has been numerically estimated to be scaled on the laser intensity as $\sim a^3$ (Lee et al., 2003b).

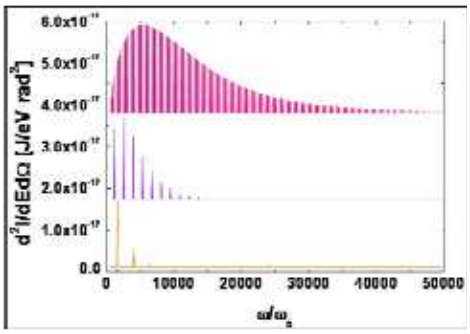

Fig. 5. Spectra of RNTS in a counter-propagating geometry for different laser intensities, a_o=0.1, 0.8, 1.6, and 5 from bottom. (The spectrum for a_o=0.1 is hardly seen due to its lower intensity.)

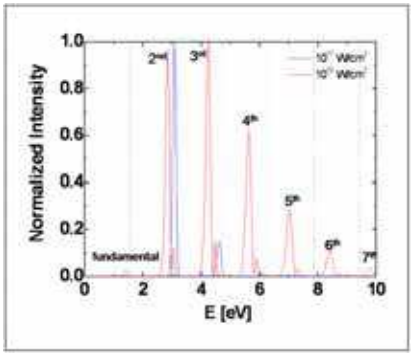

Fig. 6. Red-shift of harmonic frequencies on laser intensity. The spectra were obtained at the direction of $\theta = 90^o$ and $\phi = 0^o$ from an electron initially at rest. The vertical dotted lines indicate un-shifted harmonic lines. For this calculation, a linearly polarized laser pulse with a pulse width in full-with-half-maximum (FWHM) of 20 fs was used.

As shown in Fig. 6, the fundamental frequency, ω_1^s shifts to the red side as the laser intensity increases. This is caused by the relativistic drift velocity of the electron driven by $\vec{v} \times \vec{B}_L$ force. Considering Doppler shift, it can be obtained as (Lee et al., 2006)

$$\frac{\omega_1^s}{\omega_L} = \frac{4\gamma_o^2\left(1-\beta_{zo}\right)}{4\gamma_o^2\left(1-\vec{\beta}_o\cdot\hat{n}\right)+a_o^2\dfrac{\left(1-\cos\theta\right)}{\left(1-\beta_{zo}\right)}}. \tag{9}$$

In the case of an electron initially at rest ($\gamma_o = 1$, $\beta_o = 0$), this leads to the following formula

$$\frac{\omega_1^s}{\omega_L} = \frac{1}{1 + \frac{a_o^2}{4}(1 - \cos\theta)} . \tag{10}$$

Note that the amount of the red shift is different at different angles. The dependence on the laser intensity can be stated as follows. As the laser intensity increases, the electron's speed approaches the speed of light more closely, which makes the frequency of the laser more red-shifted in the electron's frame. No shift occurs in the direction of the laser propagation. The parasitic lines in the blue side of the harmonic lines are caused by the different amount of the red-shift due to rapid variation of laser intensity.

The angular distributions of the RNTS radiations show interesting patterns depending on harmonic orders [Fig. 7]. The distribution in the forward direction is rather simple, a dipole radiation pattern for the fundamental line and a two-lobe shape for higher order harmonics. There is no higher order harmonic radiation in the direction of the laser propagation. In the backward direction, the distributions show an oscillatory pattern on θ and the number of peaks is equal to the number of harmonic order. Thus there is no even order harmonics to the direction of $\theta = 180^o$.

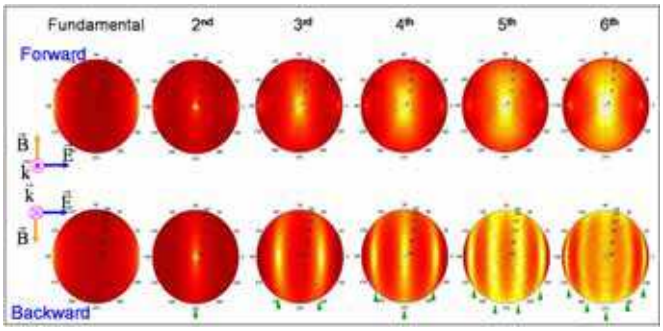

Fig. 7. Angular distributions of the RNTS harmonic radiations from an electron initially at rest. This was obtained with a linearly polarized laser pulse of 10^{18} W/cm^2 in intensity, 20 fs in FWHM pulse width. The green arrows in the backward direction indicate nodes.

For a laser intensity of 10^{20} W/cm^2 (a_o=6.4), the harmonic spectra from an electron initially at rest are plotted in Fig. 8 for different laser polarizations. In the case of a linearly polarized laser, the electron undergoes a zig-zag motion in a laser cycle. Thus the electron experiences severer instantaneous acceleration than in the case of a circularly polarized laser, in which case the electron undergoes a helical motion. This makes RNTS radiation stronger in intensity and higher in photon energy in the case of a linearly polarized laser. The most different characteristics are the appearance of a large-interval modulation in the case of a linear polarization denoted as '1' in Fig. 8 (a). This is also related with the zig-zag motion of the electron during a single laser cycle. During a single cycle, the electron's velocity becomes zero instantly, which does not happen in the case of the circular polarization. Thus a double peak radiation appears in a single laser cycle as shown in Fig. 9 (a). Such a double peak structure in the time domain makes the large-interval modulation in the energy spectrum. In

both cases, there are modulations with small-interval denoted by '2' in the Fig. 8 (a) and (b). This is caused by the variation of the laser intensity due to ultra-short laser pulse width. Such an intensity variation makes the drift velocity different for each cycle then the time interval between radiation peaks becomes different in time domain, which leads to a small-interval modulation in the energy spectrum.

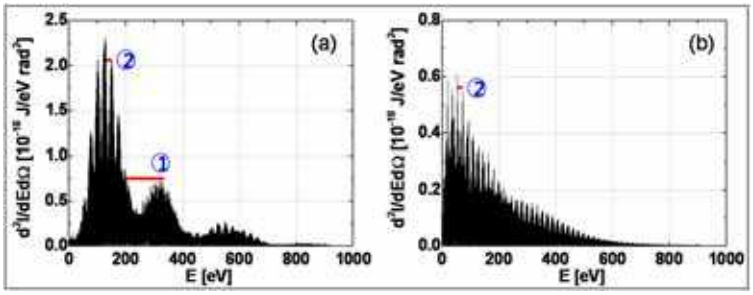

Fig. 8. RNTS spectra from an electron initially at rest on laser polarizations: (a) linear and (b) circular. The laser intensity of 10^{20} W/cm^2 (a_o=6.4) and the FWHM pulse width of 20 fs were used. Note that harmonic spectra are deeply modulated. See the text for the explanation.

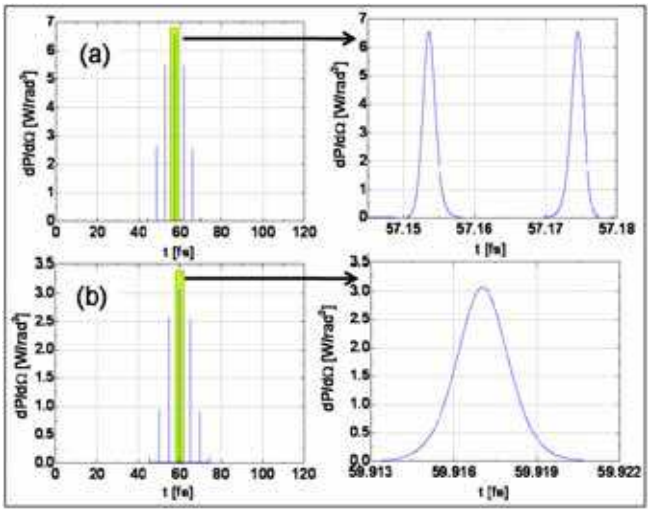

Fig. 9. Temporal shape of the RNTS radiations on polarizations with the same conditions as in Fig. 8: (a) linear and (b) circular polarization. The figures on the right hand side are the zoom-in of the marked regions in green color.

The temporal structure or the angular power can be seen in Fig. 9. As commented above, in the case of the linear-polarization, it shows a double-peak structure. One can also see that the pulse width of each peak is in the range of attosecond. This ultra-short nature of the RNTS radiation makes RNTS deserve a candidate for as an ultra-short intense high-energy photon source. The pulse width is proportional to the inverse of the band width of the harmonic spectrum, and thus scales on the laser intensity as $\sim a^{-3}$ (Lee et al., 2003b). The peak power is analytically estimated to scale $\sim a^5$ (Lee et al., 2003b).

The zig-zag motion of an electron under a linearly polarized laser pulse makes the radiation appears as a pin-like pattern in the forward direction as shown in Fig. 10 (a). However the radiation with a circularly polarized laser pulse shows a cone shape [Fig. 10 (b)] due to the helical motion of the electron. The direction of the peak radiation, θ_p was estimated to be $\theta_p \approx 2\sqrt{2} / a_o$ (Lee et al., 2006).

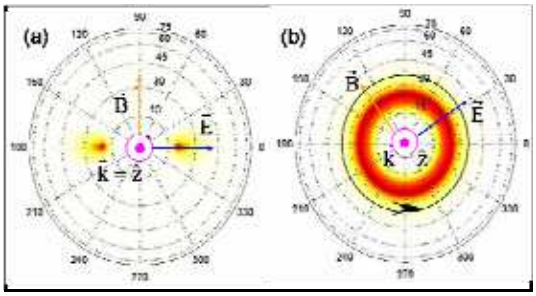

Fig. 10. Angular distributions of the RNTS radiations for different polarizations (a) linear and (b) circular polarization. The laser intensity of 10^{20} W/cm^2 (a_o=6.4) and the FWHM pulse width of 20 fs are used as in Fig. 8.

3. Coherent RNTS radiations

In the previous section, fundamental characteristics of the RNTS radiation are investigated in the case of single electron. It was also shown that the RNTS radiation can be an ultra-short radiation source in the range of attosecond. To maintain this ultra-short pulse width or wide harmonic spectrum even with a group of electrons, it is then required that the radiations from different electrons should be coherently added at a detector. In the case of RNTS radiation, which contains wide spectral width, such a requirement can be satisfied only if all the differences in the optical paths of the radiations from distributed electrons to a detector be almost the same. This condition can be practically restated: all the time intervals that scattered radiations from different electrons take to a detector, Δt_{int} should be comparable with or less than the pulse width of single electron radiation, Δt_{rad} as shown in Fig. 11. In the following subsections, two cases of distributed electrons, solid target and elelctron beam will be investigated for the coherent RNTS radiations.

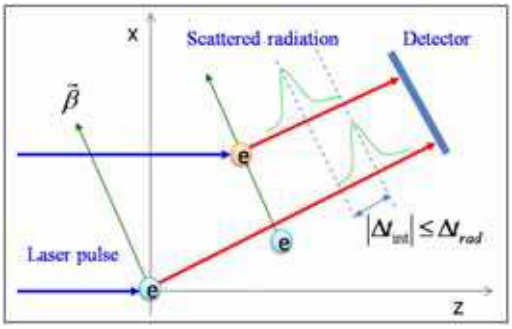

Fig. 11. Schematic diagram for the condition of coherent RNTS radiation.

3.1 Solid target

In the case of a solid target for distributed electrons (Lee et al, 2005), the time intervals that radiations take to a detector can be readily obtained with the following assumptions as the first order approximation: (1) plane wave of a laser field, (2) no Coulomb interaction between charged particles, thus neglecting ions, and (3) neglect of initial thermal velocity distribution of electrons during the laser pulse. With these assumptions, the radiation field $\vec{f}_i(t)$ by an electron initially at a position, $\vec{r}_i$, due to irradiation of an ultra-intense laser pulse propagating in the +z direction can be calculated from that of an electron initially at origin, $\vec{f}_o(t)$ by considering the time intervals between radiations from the electron at $\vec{r}_i$ and one at origin, Δt_i,

$$\Delta t_i = \Delta t'_i - \frac{\hat{n}\cdot\vec{r}}{c}, \tag{11}$$

where $\Delta t'_i = z_i / c$ is the time which the laser pulse takes to arrive at the i-th electron from origin: $\vec{f}_i(t) = \vec{f}_o(t - \Delta t_i)$. Then all the radiation fields from different electrons are summed on a detector to obtain a total radiation field, $\vec{F}(t)$ as

$$\vec{F}(t) = \sum_i \vec{f}_o(t - \Delta t_i). \tag{12}$$

The condition for a coherent superposition in the z-x plane can now be formulated by setting Eq. (11) to be less than or equal to the pulse width of single electron radiation, Δt_{rad}. This leads to the following condition [See Fig. 12]:

$$\left| z\tan\xi - x \right| \le \frac{c\Delta t_{rad}}{\sin(2\xi)}. \tag{13}$$

Equation (13) manifests that RNTS radiations are coherently added to the specular direction of an incident laser pulse off the target, if the target thickness, T_{hk} is restricted to

$$T_{hk} \le \frac{c\Delta t_{rad}}{\sin\xi}. \tag{14}$$

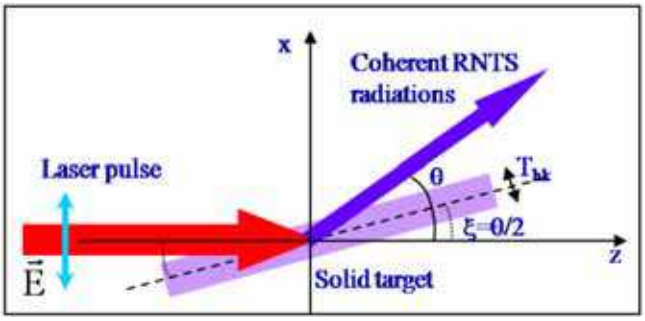

Fig. 12. Schematic diagram for a coherent RNTS condition with an ultrathin solid target.

Since the incident angle of the laser pulse can be set arbitrarily, one can set θ to the direction of the radiation peak of single electron, θ_p. For a linearly polarized laser with an intensity of 4x10[19] W/cm[2], and a pulse duration of 20 fs FWHM, $\theta_p = 27^o$ and $\Delta t_{rad} = 5$ attosecond for a single electron. Equation (14) then indicates that the target thickness should be less than 7 nm. With these laser conditions, harmonic spectra were numerically obtained to demonstrates the derived coherent condition [Fig. 13].

The spectra in Fig. 13 (a) were obtained for a thick cylindrical target of 1 μm in thickness and radius, and 10^{18} cm^{-3} in electron density under the normal incidence of a laser on its base. The spectrum in Fig. 13 (b) is for the case of oblique incidence on an ultra-thin target of 7 nm in thickness, 5 μm in width, 20 μm in length, 10^{16} cm^{-3} in electron density, and $\xi = 13.5^o$, which were obtained with Eqs. (13) and (14). From Fig. 13 (b), which corresponds to the condition for coherent RNTS radiation, one can find that the spectrum from thin film (a group of electrons) has almost the same structure as that from a single electron radiation [Inset in Fig. 13 (b)] in terms of high-energy photon and a modulation. On the other hand, in the case of Fig. 13 (a), the harmonic spectra show much higher intensity at low energy part, which is caused by an incoherent summation of radiations.

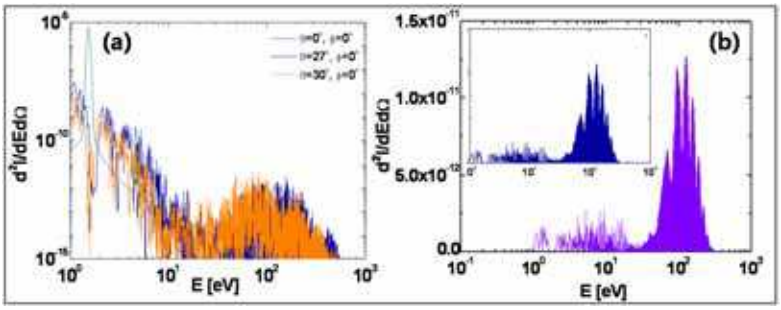

Fig. 13. RNTS spectra obtained under (a) incoherent and (b) coherent conditions. In (a), the spectra obtained in three different directions are plotted, while (b) were obtained in the specular direction. One can see that the spectrum in the coherent condition is very similar with that obtained from single electron calculation (inset of (b)).

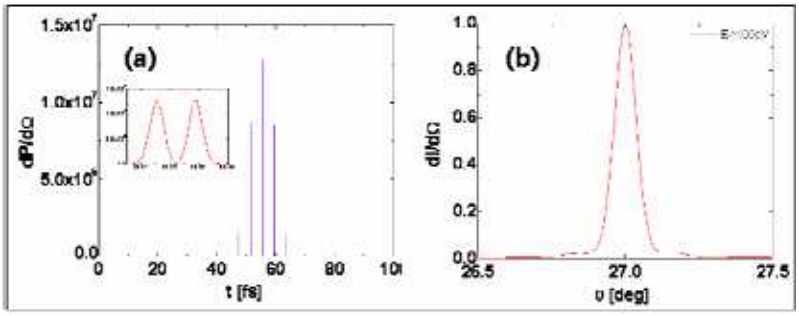

Fig. 14. (a) Temporal shape and (b) angular distribution in the case of the coherent condition [Fig. 13 (b)].

The temporal shape at the specular direction for the case of coherent condition [Fig. 13 (b)] is plotted in Fig. 14 (a), which shows an attosecond pulse. The direction-matched coherent condition also leads to a very narrow angular divergence as shown in Fig. 14 (b). It should be mentioned that with a thick cylinder target, the radiation peak appears at $\theta = 0^o$, because the dipole or fundamental radiation becomes dominant in that direction.

3.2 Electron beam

Exploiting a solid target for a coherent RNTS radiation may involve a complicated plasma dynamics due to an electrostatic field produced by a charge separation between electrons and ions. Instead, an idea using an electron beam has been proposed (Lee et al., 2006).

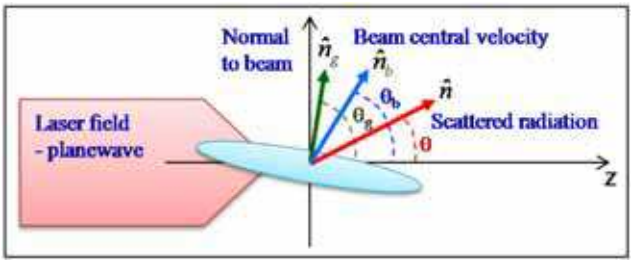

Fig. 15. Schematic diagram for the analysis of a coherent RNTS radiation with an electron beam.

Following similar procedure in the previous section, the RNTS harmonic spectrum can be obtained with that from an electron at center and its integration over initial electron distributions with phase relationships as

$$\vec{A}(\omega) \approx \vec{A}_c(\omega) \int dV_o f\left(\vec{r}_o, \vec{\beta}_o\right) \exp\left(i\delta \frac{\omega}{\omega_o}\right), \tag{15}$$

where $\vec{A}_c(\omega)$ is the angular spectral field from the central electron. The $\delta / k_o = \left(1 - \hat{n} \cdot \vec{\beta}_o\right) / \left(1 - \beta_{oz}\right) z - \hat{n} \cdot \vec{r}_o$ represents the phase relations between scattered radiations due to different initial conditions of the electrons. The distribution function can be assumed to have a Gaussian profile with cylindrical symmetry:

$$f\left(\vec{r}_o, \vec{\beta}_o\right) = \frac{N}{(2\pi)^3 R^2 L \sigma_\Gamma \sigma_{\beta'}^2} \exp\left[-\frac{x_o^{\,2} + y_o^{\,2}}{2R^2} - \frac{z_o^{\,2}}{2L^2}\right] \times \exp\left[-\frac{\beta_{ox}^2 + \beta_{oy}^2}{2\beta_b^2 \sigma_{\beta'}^2} - \frac{\left(\gamma_o - \gamma_b\right)^2}{2\gamma_b^2 \sigma_\Gamma^2}\right], \tag{16}$$

where the following parameters are used: the number of electrons (N), radius (R), length (L), fractional energy spread (σ_Γ), and divergence ($\sigma_{\beta'}$). γ_b is the relativistic gamma factor of the beam, and β_b its corresponding velocity divided by the speed of light. In the above formula, the beam velocity and the axis of the spatial distribution of the beam have the same directions and directed to +z, but below, the direction of the beam velocity ($\hat{n}_b$) and the axis of the beam ($\hat{n}_g$) are allowed to have different directions, as shown in Fig. 15. The integration of Eq. (15) by taking the first order of ($\vec{\beta}_b - \vec{\beta}_o$) in δ leads to the following formula for the coherent spectrum:

$$\vec{A}(\omega) \approx NF(\omega)\vec{A}_c(\omega), \tag{17}$$

$$F(\omega) \approx \frac{1}{\sqrt{1+k^2l^2}} \exp\left[-\frac{k^2}{2(1+k^2l^2)}\left(Q_r^2+Q_\beta^2\right)\right], \tag{18}$$

$$Q_r^2 = L^2N_{gz}^2 + R^2\left(N_{gx}^2+N_{gy}^2\right), \tag{19}$$

$$Q_\beta^2 = k^2R^2T^2\left[L^2\left(N_{gx}n_{gz}-N_{gz}n_{g\theta z}\right)^2 + N_{gy}^2\left(R^2n_{g\theta z}^2+L^2n_{gz}^2\right)\right], \tag{20}$$

with $k = \omega / c$ and the other parameters being

$$l^2 = T^2\left(L^2n_{gz}^2 + R^2n_{g\theta z}^2\right), \tag{21}$$

$$T^2 = \left(\frac{\beta_b}{1-\beta_{bz}}\right)^2\left(\frac{\sigma_\Gamma^2}{\left(\gamma_b^2-1\right)^2}N_{bz}^2 + \sigma_{\beta'}^2\left(N_{bx}^2+N_{by}^2\right)\right), \tag{22}$$

$$\vec{N}_s = \vec{\vec{M}}_s \cdot \left(\hat{n} - p_b\hat{z}\right), \tag{23}$$

$$\vec{\vec{M}}_s^T = \left[\hat{n}_{s\theta} \quad \hat{n}_{s\varphi} \quad \hat{n}_s\right], \tag{24}$$

$$p_b = \frac{1-\vec{\beta}_b\cdot\hat{n}_r}{1-\beta_{bz}}. \tag{25}$$

In Eqs. (23) and (24), the subscript, 's' represents either 'g' or 'b'. $\hat{n}_{s\theta}$ and $\hat{n}_{s\varphi}$ are two unit vectors perpendicular to $\hat{n}_s$. Equation (18) or the coherent factor, $F(\omega)$ shows that, as the beam parameters get larger, the coherent spectrum disappears from high frequency. This manifests that the phase matching condition among electrons is severer for high frequencies.

For the radiation scattered from an electron beam to be coherent up to a frequency ω_c, the above coherent factor $F(\omega)$, should be almost 1, or the exponent should be much smaller than 1 in the desired range of frequency. In the z-x plane, $N_{gy} = 0$; then, this leads to the following relations, one for the angular relation:

$$N_{gx} = \sin\left(\theta-\theta_g\right) + \sin\theta_g\frac{1-\beta_b\cos\left(\theta_b-\theta\right)}{1-\beta_b\cos\theta_b} = 0, \tag{26}$$

and the other for the restriction on the electron beam parameters:

$$k_cLN_{gz}\sqrt{\frac{1+k_c^2R^2T^2\sin^2\theta_g}{1+k_c^2l^2}} < 1. \tag{27}$$

Eq. (26) also shows why the direction of the beam velocity (θ_b) is set to be different from the axis of the beam distribution (θ_g); otherwise, N_{gx} cannot be zero. The physical meaning of Eqs. (26) and (27) is that time delays between electrons should be less than the pulse width generated by a single electron as commented in the previous section. This equation can be used to find θ_g for given θ_b and θ which can be set to the optimal condition obtained from the single electron calculation. For the realization of the coherent condition, the most important things are the length of the electron beam (L) and the condition to minimize N_{gz}. To minimize N_{gz}, θ should be near 0o but not 0o at which only dipole radiation appears. From single electron calculation, it has been found that when $\theta_b \approx 0^o$ or in the case of a co-propagation (laser and electron beam propagate near the same direction), such a condition can be fulfilled.

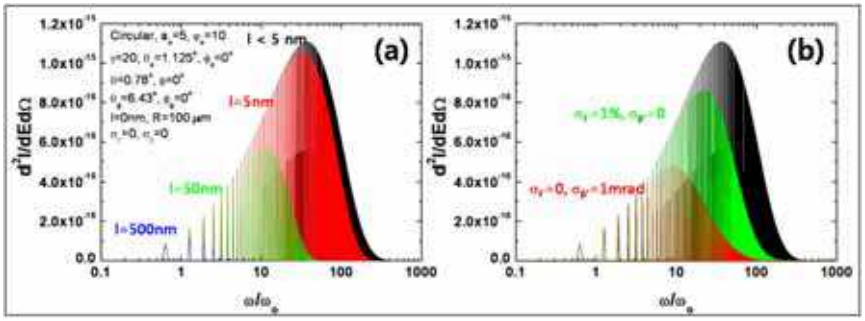

Fig. 16. Coherent RNTS radiation spectra for different beam parameters: (a) beam length and (b) other beam parameters. For better view, only envelops are plotted.

From the single electron calculation (the radiation from an electron of γ_0 = 20 under irradiation of a circularly polarized laser of a_o = 5), it has been found that the peak radiation appears at $\theta = 0.78^o$ when $\theta_b = 1.125^o$. The insertion of these data into Eq. (26) and (27) leads to $\theta_g = 6.43^o$ and the beam length being restricted to a few nanometers. Coherent RNTS spectra for different electron beam parameters are plotted in Fig. 16. As expected, one can see that the coherent spectral intensity decreases at high frequencies as the beam length increases. These calculations show that the coherent conditions for the beam length and beam divergence are most stringent. However, with a moderate condition, the broadening of the coherent spectrum is still enough to generate about a 100-attosecond pulse.

4. Effects of the high-order laser fields under tight-focusing condition

Paraxial approximation is usually used to describe a laser beam. However, when the focal spot size gets comparable to the laser wavelength, it cannot be applied any more. This is the situation where the RNTS actually takes place. A tightly-focused laser field and its effects on the electron dynamics and the RNTS radiation will be discussed in this section.

4.1 Tightly focused laser field

The laser fields propagating in a vacuum are described by a wave equation. The wave equation can be evaluated in a series expansion with a diffraction angle, $\varepsilon = w_0 / z_r$, where w_0 is beam waist and z_r Rayleigh length. It leads to the following formulas for the laser

fields having linear polarization in the x-direction (zeroth-order) and propagating in the +z direction (Davis, 1979; Salamin, 2007),

$$E_x = E\left\{S_0 + \epsilon^2\left[\xi^2 S_2 - \frac{\rho^4 S_3}{4}\right] + \epsilon^4\left[\frac{S_2}{8} - \frac{\rho^2 S_3}{4} - \frac{\rho^2(\rho^2 - 16\xi^2)S_4}{16} - \frac{\rho^4(\rho^2 + 2\xi^2)S_5}{8} + \frac{\rho^8 S_6}{32}\right]\right\}, \quad (28)$$

$$E_y = E\xi\upsilon\left\{\epsilon^2[S_2] + \epsilon^4\left[\rho^2 S_4 - \frac{\rho^4 S_5}{4}\right]\right\}, \quad (29)$$

$$E_z = E\xi\left\{\epsilon[C_1] + \epsilon^3\left[-\frac{C_2}{2} + \rho^2 C_3 - \frac{\rho^4 C_4}{4}\right] + \epsilon^5\left[-\frac{3C_3}{8} - \frac{3\rho^2 C_4}{8} + \frac{17\rho^4 C_5}{16} - \frac{3\rho^6 C_6}{8} + \frac{\rho^8 C_7}{32}\right]\right\}, \quad (30)$$

$$B_x = 0, \quad (31)$$

$$B_y = E\left\{S_0 + \epsilon^2\left[\frac{\rho^2 S_2}{2} - \frac{\rho^4 S_3}{4}\right] + \epsilon^4\left[-\frac{S_2}{8} + \frac{\rho^2 S_3}{4} + \frac{5\rho^4 S_4}{16} - \frac{\rho^6 S_5}{4} + \frac{\rho^8 S_6}{32}\right]\right\}, \quad (32)$$

$$B_z = E\upsilon\left\{\epsilon[C_1] + \epsilon^3\left[\frac{C_2}{2} + \frac{\rho^2 C_3}{2} - \frac{\rho^4 C_4}{4}\right] + \epsilon^5\left[\frac{3C_3}{8} + \frac{3\rho^2 C_4}{8} + \frac{3\rho^4 C_5}{16} - \frac{\rho^6 C_6}{4} + \frac{\rho^8 C_7}{32}\right]\right\}. \quad (33)$$

The laser fields are written up to the 5th order in ε. In above equations, $E = E_o(w/w_o)g(t - z/c)\exp(-r^2/w^2)$, $w = w_0\sqrt{1 + (z/z_r)^2}$, $z_r = \pi w_0^2/\lambda$, $\xi = x/w_0$, $\upsilon = y/w_0$, $\zeta = z/z_r$, and $\rho^2 = \xi^2 + \upsilon^2$. $g(t - z/c)$ is a laser envelop function. C_n and S_n are defined as

$$\begin{aligned} C_n &= \left(\frac{w_0}{w}\right)^n \cos(\psi + n\psi_G); \qquad n = 0,1,2,3\ldots, \\ S_n &= \left(\frac{w_0}{w}\right)^n \sin(\psi + n\psi_G), \end{aligned} \quad . \quad (34)$$

where $\psi = \psi_0 + \omega t - kz - kr^2/2R + \psi_G$ and $R = z + z_r^2/z$. ψ_0 is a constant initial phase and k is the laser wave number, $2\pi/\lambda$. ψ_G is the Gouy phase expressed as

$$\psi_G = \tan^{-1}\frac{z}{z_r}. \quad (35)$$

The zeroth order term in ε is a well known Gaussian field. One can see when ε cannot be neglected: when the focal size gets comparable to the laser wavelength, a field longitudinal to the propagation direction appears and the symmetry between the electric and the magnetic fields is broken.

Because ε is proportional to $1/w_0$, the high order fields (HOFs) become larger for smaller beam waist. Figure 17 shows that E_y and E_z get stronger as w_o decreases. The peak field strengths of E_y and E_z amount to 2.6% and 15% of E_x at w_o = 1 μm, respectively. In the case of a counter-interaction between an electron and a laser pulse, HOFs much weaker than the zeroth-order field does not affect the electron dynamics. However, when the relativitic electron is driven by a co-propagating laser pulse, weak HOFs significantly affect the electron dynamics and consequently the RNTS radiation.

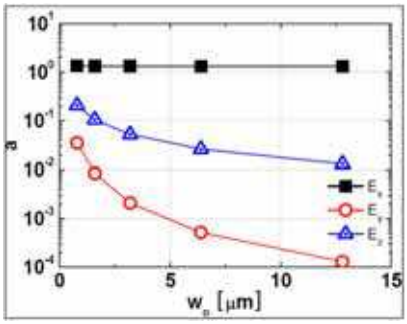

Fig. 17. The strength of laser electric fields against the beam waist size are plotted in unit of the normalized vector potential. The laser field is evaluated at ($w_0/2$, $w_0/2$, 0) with the zeroth-order laser intensity of a_0 = 2.2.

4.2 Dynamics of an electron electron with a tightly focused laser

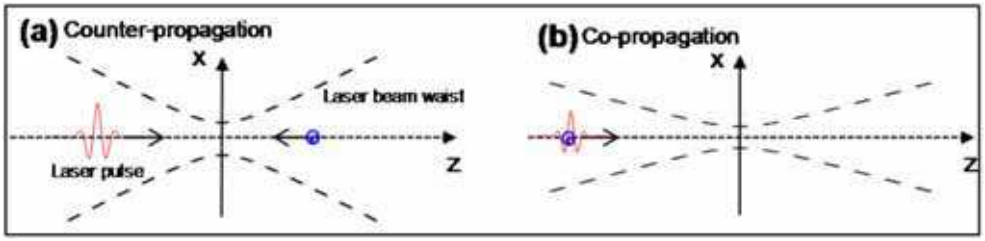

Fig. 18. Two interaction schemes between a relativistic electron and a laser pulse:
(a) counter-propagation and (b) co-propagation.

The dynamics of a relativistic electron under a tightly-focused laser beam is investigated by the Lorentz force equation [Eq. (1)]. One can consider two extreme cases of interaction geometry as shown in Fig. 18. The counter-propagation scheme, or Compton back-scattering scheme is usually adopted to generate monochromatic x-rays. It has been shown in the previous section that the co-propagation scheme is more appropriate to generate the coherent RNTS radiation. For such schemes, the effect of HOFs will be investigated.

In the z-x plane, $E_y = B_z = 0$, then the Lorentz force equation for γ and β_x (transverse velocity) in the case of the counter-propagation scheme ($\vec{\beta} \approx -1\hat{z}$), can be approximated as,

$$\frac{d\gamma}{d\tau} \approx a_0 \beta_x - a_{odd}^H , \tag{36}$$

$$\frac{d(\gamma\beta_x)}{d\tau} \approx 2a_0 + \left(a_{even}^H + b_{even}^H\right), \tag{37}$$

where $\tau = \omega_L t$, a_0 is the zeroth-order laser field in unit of the normalized potential. a_{odd}^H is odd HOFs of electric field (or longitudinal electric fields). a_{even}^H and b_{even}^H are even HOFs of electric and magnetic fields, respectively [see Eqs. (28)-(33)]. From above equations, γ can be analytically obtained considering only the first HOF as